Enhanced interfacial adhesion and osseointegration of anodic TiO_2 nanotube arrays on ultra-fine-grained titanium and underlying mechanisms

Nan Hu[1,#], Yuzheng Wu[1,4,#], Lingxia Xie[1], Shahir Mohd Yusuf[2], Nong Gao[2], Marco J. Starink[2], Liping Tong[1,], Paul K. Chu[3,*], Huaiyu Wang[1,*]*

[1] Institute of Biomedicine and Biotechnology, Shenzhen Institutes of Advanced Technology, Chinese Academy of Sciences, Shenzhen 518055, China

[2] Engineering Materials group, University of Southampton, Southampton SO17 1BJ, UK

[3] Department of Physics, Department of Materials Science and Engineering, and Department of Biomedical Engineering, City University of Hong Kong, Tat Chee Avenue, Kowloon, Hong Kong, China

[4] Shenzhen College of Advanced Technology, University of Chinese Academy of Sciences, Shenzhen 518055, China

Abstract

The poor adhesion of anodic TiO_2 nanotubes (TNTs) arrays on titanium (Ti) substrates

adversely affects applications in many fields especially biomedical engineering. Herein, an efficient strategy is described to improve the adhesion strength of TNTs by performing grain refinement in the underlying Ti substrate *via* high-pressure torsion processing, as a larger number of grain boundaries can provide more interfacial mechanical anchorage. This process also improves the biocompatibility and osseointegration of TNTs by increasing the surface elastic modulus. The TNTs in length of 0.4 μm have significantly larger adhesion strength than the 2.0 μm long ones because the shorter TNTs experience less interfacial internal stress. However, post-anodization annealing reduces the fluorine concentration in TNTs and adhesion strength due to the formation of interfacial cavities during crystallization. The interfacial structure of TNTs/Ti system and the mechanism of adhesion failures are further investigated and discussed.

Keywords: TiO_2 nanotubes; High-pressure torsion; Adhesion strength; Ultra-fine-grained materials; Ti-based implants

1. Introduction

Self-assembled TiO_2 nanotubes (TNTs) fabricated by electrochemical anodization are commonly used in photocatalytic systems, electronic devices, solar cells, sensors, as well as biomedical implants [1–10] but the poor adhesion between the TNTs and Titanium (Ti) substrate has hampered wider applications [11–18]. The weak adhesion can be ascribed to fluoride (F^-) ions [14,19–21] and internal stress [11,13,15,16] at the interface. F^- ions play a key role in the transition of compact oxide to self-organized nanotubes by dissolving TiO_2 and binding ejected Ti^{4+} at the oxide/electrolyte interface [22], forming a soluble fluoride-rich (Ti-O-F or Ti-F complexes) interface [19–21], which separates the substrate from the bottom of nanotubes and results in poor adhesion [14]. Furthermore, during the formation of TNT layers, length expansion can be observed beyond that of the oxide layer corresponding to the Pilling–Bedworth ratio (PBR) [17], which is determined by the volume ratio of oxide to the consumed metal. The reported expansion factors when converting Ti to TiO_2 nanotubes are in the range of 2.7–3.1 [23], which are much higher than the PBRs of titanium dioxide, namely 1.93 for anatase, 1.76 for rutile, and 2.4 for the amorphous phase [24]. It consequently leads to the volume difference and stress between the TNT layer and Ti substrate [24,25]. The large internal stress in the oxide layer generates an upward force at the nanotube bottom and decreases the bonding strength between the TNTs and substrate [26].

There have been efforts to increase the adhesion strength of TNTs and most of the experiments have aimed at reducing the influence of the fluoride-rich layer and internal stress or strengthening the Ti-TiO_2 bonding [17,27–30]. In particular, annealing is an

efficient way to reduce the concentration of F^- in the TNT layers [28,29] while preserving the self-organized morphology of TNT layers. Annealing can also improve the crystallinity of TNT layers because the as-anodized amorphous TNT layers [2,31,32] can be converted into crystalline anatase or rutile phases [28,31,33], possibly leading to improved cell adhesion and proliferation [34]. But so far, the inflence of annealing on the adhesion strength of TNTs on Ti is not well understood. Recently, a different strategy to enhance the adhesion strength of anodic TNT layers has been proposed by refining the grain size of the Ti-6Al-4V substrate to the sub-micrometer or nanometer range *via* high pressure torsion (HPT) [35]. HPT is a severe plastic deformation (SPD) method to obtain nanostructured metallic materials with better mechanical properties [36–38]. However, it remains unclear whether the improved adhesion is associated with the larger number of defects induced by HPT which enhances the mechanical anchorage between the coating and the ultra-fine-grained (UFG) substrate, or HPT that produces monophasic TNTs on the dual-phasic Ti alloy substrate thereby reducing the stress concentration in the TNT layers.

In this study, pure Ti consisting of a single α-phase is used to exclude the influence of secondary phases and alloying elements, and the effects of grain-size refinement on the adhesion strength of anodic TNT layers before and after annealing are assessed systematically. Furthermore, the mechanical properties of cellular environment are recognized as significant regulators of the fate of stem cells [39] and mechano-transduction of cells is contributed by critical mechanosensitive molecules and cellular components such as integrins, stretch-activated ion channels, and cytoskeletal filaments [40]. Hence, in addition to the grain refinement effects on the surface mechanical properties of TNT layers [38], the influence on adhesion, proliferation and osteogenic differentiation of human

mesenchymal stem cells (HMSCs) is also investigated.

2. Material and methods

2.1 Processing and characterization of Ti substrate

2.1.1 HPT processing

A commercially pure (CP) titanium (grade 2) extruded bar was used. Prior to HPT processing, a CP Ti bar with a diameter of 10 mm was cut and ground into disks with a thickness between 0.80-0.85 mm. The disks were annealed at 800 ºC for 8 h to obtain equiaxed grains and designated as coarse-grained "CG". The CG disks were then processed by HPT under quasi-constrained condition using two anvils at a pressure of 3 GPa and torsional straining was applied through rotation of the lower anvil up to 10 turns [41]. The process produced very high equivalent strain ε of about 6 [41,42] and the Ti samples after HPT processing had an ultra-fine-grained structure and designated as "UFG".

2.1.2 Grain size measurement

The samples were ground with SiC abrasive papers of 120, 800, 1200 and 4000 grit, polished with 6 μm and 1 μm diamond paste (Struers), and etched in a solution containing HF, HNO_3 and H_2O with a volume ratio of 2:3:10. The optical microscopy (OM, Olympus BX41M-LED) was employed and a linear intercept method was adopted for the grain size measurement using the OM images of the CG samples. A JEM 3010 transmission electron microscope (TEM) was used to measure the grain size of UFG samples at 300 kV. The TEM samples were prepared by twin-jet electropolishing at 30 V in a solution containing

6% $HClO_4$ + 4% H_2O + 90% ethanol at -30 to -25 °C. Selected-area electron diffraction (SAED) was performed on the TEM sample with a spot size of 360 nm.

2.2 Processing and characterization of TNTs

2.2.1 Electrochemical anodization

The Ti samples were the anodes in a two-electrode cell with a pure Ti bar as the cathode and a nonaqueous electrolyte containing 0.25 wt% NH_4F (Riedel-de Haën), 98.75 wt% glycerol (Alfa Aesar), and 1 wt% deionized water. A circular area with a diameter of 0.6 mm on the anode was exposed to the electrolyte to produce TNT layers. The distance between the electrodes was 1 cm and a constant direct current voltage of 30 V was applied. Two anodization procedures were implemented to obtain long and short TNTs. The long TNTs were fabricated by a two-step anodization process. The first step was carried out for 16 h at 30 V to form a preliminary TNT layer which was subsequently peeled off. The second anodization step was carried out for 6 h at 30 V and the short TNTs were fabricated in the same setup by one-step anodization for 1 h. The anodization experiments were performed at room temperature and after anodization the samples were rinsed in deionized water for 1 min to remove the residual electrolyte. Subsequently, half of the anodized Ti samples were annealed in air at 350 ºC for 1 h. The sample designations are given in Table 1.

Table 1. Designation of the different TNTs on Ti samples.

	TNT-L (Long TNTs)		**TNT-S (Short TNTs)**	
On CG sample	*CG-TNT-L*	*CG-TNT-L-A*	*CG-TNT-S*	*CG-TNT-S-A*
On UFG sample	*UFG-TNT-L*	*UFG-TNT-L-A*	*UFG-TNT-S*	*UFG-TNT-S-A*
Anodization procedures	First step for 16 h and second step for 6 h	First step for 16 h and second step for 6 h and annealed at 350 ºC for 1h	One step for 1 h	One step for 1 h and annealed at 350 ºC for 1h

2.2.2 Scanning electron microscopy

After anodization, the TNT layers were mechanically detached from the substrate during nanoscratch tests and examined by field-emission scanning electron microscopy (SEM, JEOL JSM 6500) in the secondary electron mode and energy-dispersive X-ray spectroscopy (EDS, Oxford accessory). The average and standard deviations of parameters including the layer thickness and bottom diameter were calculated based on 400 randomly selected nanotubes using the NanoMeasurer 1.2 software. The observation of nanoscratch tracks as well as failure analysis were also carried out by SEM.

2.2.3 Transmission electron microscopy

Thin disks in 3 mm diameter were cut from the HPT substrate 3.5 mm from the center for metallographic grinding, polishing, and twin-jet electro-polishing at -30 ˚C with a mixture of 6 vol% perchloric acid, 60 vol% methanol, and 34 vol% butanol. The microstructure was observed by transmission electron microscopy (TEM, JEM 3010) at 300 kV. The grain diameter was estimated by averaging the length and width of the

strongly diffracting grains using the ImageJ® image analysis software [46]. Selected-area electron diffraction (SAED) was performed from a spot size of 360 nm.

2.2.4 X-ray diffraction

The TNT layers were examined by X-ray diffraction (XRD) and compared to the Ti substrate. Prior to XRD, the Ti substrate was ground with a 4000-grit abrasive paper and rinsed with ethanol. XRD was conducted on a Bruker D2 Phaser diffractometer using Cu K_α radiation at 30 kV and 10 mA with a step size of 0.02° and step time of 0.25 s between 20° and 90° (2θ). To improve the accuracy, the data were collected from 3 separate scans and a DIFFRAC EVA software was used to identify the peak intensity and location. XRD profile broadening analysis was conducted using the Rietveld method with the 'Materials Analysis using Diffraction' (MAUD) software [43,44]. In MAUD, the parameters of incident radiation and dimensions were set as follows: α_1 = 1.5406 μm, α_2=1.54439 μm, weight ratio = 0.5, and goniometer radius = 141 μm.

2.2.5 Differential scanning calorimetry

The long TNT layers formed by two-stage anodization were evaluated by differential scanning calorimetry (DSC). The TNT layers were mechanically peeled off, sealed in an aluminum pan, and placed in a Perkin-Elmer Pyris-1 calorimeter with an empty sealed aluminum pan as the reference. A heating rate of 30 ºC min^{-1} was adopted and the experiment was carried out in nitrogen. The DSC thermographs were corrected by subtracting a baseline obtained from the DSC run with an empty pan and three-point correction was implemented to correct data for experimental factors including the baseline

curvature [45].

2.2.6 X-ray photoelectron spectroscopy

X-ray photoelectron spectroscopy (XPS) was performed on an ESCALAB 250Xi (Thermo Fisher) XPS system with monochromatic Al K_α X-ray (1486.6 eV). The binding energies of Ti 2p, O 1s, F 1s, N 1s, and C 1s were determined at a pass energy of 50 eV with a resolution of 0.1 eV using the binding energy of C 1s (284.8 eV) as the reference.

2.2.7 Nanoscratch test

The nanoscratch tests were performed on a Keysight Nano Indenter G200 equipped with a cube corner indenter tip and calibrated by the nanoindentation measurements using a fused silica reference sample over a wide load range. The tests were performed with linearly increasing loads from 0 to 100.00 mN at a speed of 10 μm/s up to 500 μm. At least 3 nanoscratch tests were performed for each sample and the test locations were at least 50 μm apart.

2.2.8 Wettability test

The contact angles were determined by the sessile drop method on an Attention Theta Lite contact angle meter (Biolin Scientific, Linthicum Heights, MD, USA). Placement of the deionized water droplets (4 μL) was controlled by a Hamilton syringe and data collection was manually triggered by the initial contact on the solid surface. The images were automatically analyzed using One Attension software, Version 1.8 (Biolin Scientific) to identify the baseline and calculate the contact angles.

2.2.9 Cell viability

HMSCs were obtained from the American Type Culture Collection (ATCC) and maintained in the culture medium composed of the 89% α-MEM basic medium (Hyclone), 10% fetalbovine serum (Corning), and 1% penicillin-streptomycin (Invitrogen). In the biological assays, the HMSCs were seeded on the samples at a density of 2×10^4 cells per sample on 24-well tissue culture plates. The samples were sterilized with ultraviolet light for half an hour before cell seeding and the cell counting kit-8 (CCK-8) was used to determine the viability of HMSCs. After incubation for 4, 24, and 72 h, the cell culture medium was collected and the samples were washed three times with sterile phosphate buffer saline (PBS) solution before 400 μL of the culture medium containing 10% CCK-8 were added. After incubation for another 2 h at 37 ˚C, 200 μL of the medium in each well were transferred to another 96-well plate to measure the absorbance at a wavelength of 450 nm using a microplate reader (BL340, Biotech, USA).

2.2.10 Bone-related gene expression of HMSCs

The osteogenic differentiation-related genes of the cultured HMSCs, alkaline phosphatase (ALP), and osteocalcin (OCN) were analyzed by the quantitative real-time polymerase chain reaction (RT-PCR), with β-actin as the house-keeping gene for normalization. In brief, the cells were seeded at a density of 3×10^4 cells/sample and incubated with the osteogenic medium (basic culture medium supplemented with 50 μg/ml ascorbic acid 2 phosphate (Sigma), 10 mM β-glycerophosphate (Sigma), and 0.1 μM dexamethasone (Sigma)) for 14 days. Afterwards, the total RNA was extracted from HMSCs using trizol (Qiagen, Hilden, Germany) and reversely transcribed into cDNA by a

RevertAid First Strand cDNA Synthesis Kit (Thermo Fisher) according to the manufacturer's instruction. The expression levels of ALP, OCN and β-actin were determined on a Bio-Rad CFX 96 Real-Time System using a mixture of SYBRGreen Realtime PCR Master Mix (Toyobo) and the forward and reverse primers are listed in Table S1.

2.2.11 Statistical analysis

400 nanotubes were randomly chosen to measure the diameter of each sample and the thickness of the TNT layers were determined from three randomly chosen cross-sections with 10-time measurements over each cross-section. The critical loads for the initial and continuous spallation in nanoscratch testing were based on three repeated measurements. The *in vitro* assays were performed in triplicate and each *in vitro* experiment was repeated three times with data from a typical experiment shown. All the values were expressed as mean ± standard deviation. One-way analysis of variance (ANOVA) followed by Student-Newman-Keuls post hoc test was performed to determine the statistical significance. A difference at $^{*}p < 0.05$ was considered to be significant and that at $^{**}p < 0.01$ was considered to be highly significant.

3. Results

3.1 Grain microstructure of Ti substrate

Figure 1a shows the OM image of the CG substrate revealing a mean grain size of 33 ± 5 μm, and Figures 1b and 1c depict the bright-field and dark-field TEM images of the

edge area of the UFG substrate, respectively. After ten turns of HPT processing, the microstructure of the UFG substrate is quite homogenous with a grain size of 138 ± 53 nm. The extinction contours in the grain interior suggest significant lattice distortion associated with the high internal stress. The diffraction pattern shows numerous spots arranged in circles even with a small aperture size of 360 nm (Figure 1c inset), indicating that several grains with high angle grain boundaries are present in the small area [46] and significant spreading of spots confirms the existence of large micro-strain [47].

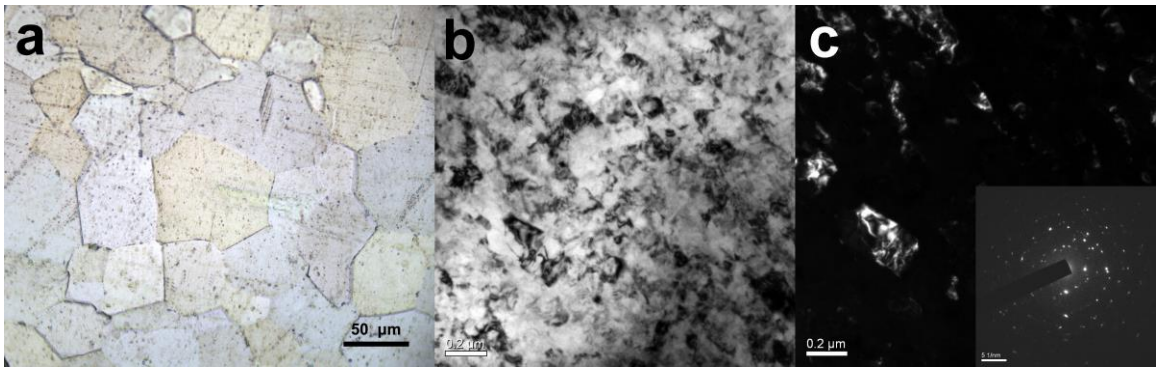

Figure 1. (a) OM images of the CG substrate. TEM images of the UFG substrate: (b) Bright-field image and (c) Dark-field image (SAED as an inset).

3.2 Morphology of TNTs

Figure 2 presents the side and bottom views of the different TNT samples. The cross-sectional SEM images in Figures 2a and 2b reveal that the thicknesses of long TNT layers are approximately 1.7 and 2.0 μm for those fabricated on the CG and HPT substrates, respectively. The bottom view discloses that the TNTs have a hexagonal arrangement as shown in Figures 2c and 2d. The average bottom diameters of the long TNTs are 56.9 ±

0.5 nm for CG-TNT-L and 54.5 ± 0.3 nm for the UFG-TNT-L samples. As reported before [41], TNTs on the UFG substrate are more homogeneous than those on the CG substrate. After annealing, the macro dimensions of the TNTs remain the same (Figures 2e and 2h), although some pits emerge from the TNT bottom (Figures 2g and 2h, indicated by the green arrows). The thickness of the short TNT layers on both the CG and HPT samples (Figures 2i and 2j) and the annealed counterparts (Figures 2m and 2n) is 0.4 μm. The average bottom diameters of the short TNTs are 59.9 ± 8.9 nm for the CG-TNT-S and 50.4 ± 5.8 nm for the UFG-TNT-S samples. Similar to the long TNTs, the morphology of the short TNTs remains unchanged after annealing except for the appearance of some pits at the bottom as indicated by the green arrows (Figures 2o and 2p).

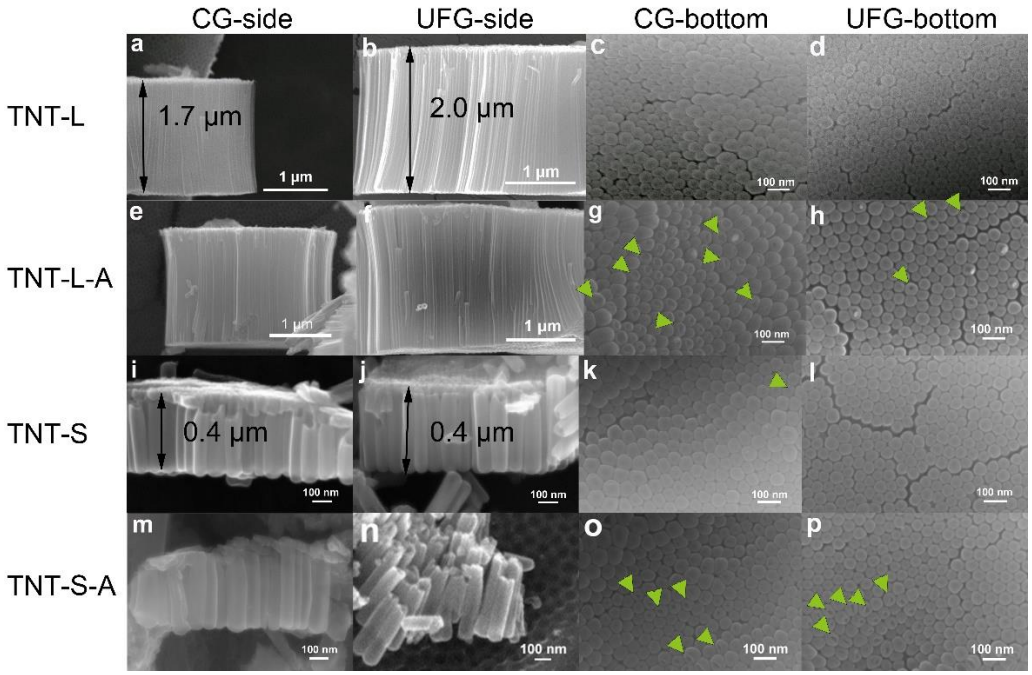

Figure 2. Side and bottom views of the TNT layers on Ti: (a, c) CG-TNT-L, (b, d) UFG-TNT-L, (e, g) CG-TNT-L-A, (f, h) UFG-TNT-L-A, (i, k) CG-TNT-S, (j, l) UFG-TNT-S, (m, o) CG-TNT-S-A and (n, p) UFG-TNT-S-A.

3.3 Growth mechanism of TNTs

The influence of the substrate grain size on the growth mechanism of TNTs is monitored *in situ* by recording the current density-time (*j*-*t*) curve and the corresponding time derivative [48], as shown in Figures 3a and 3b. As a result of the competition between oxide formation and dissolution, the morphology of TNTs is reflected by the curves. Formation of TNTs follows the reaction [19]:

$$\mathrm{Ti} + 2\mathrm{H_2O} \rightarrow \mathrm{TiO_2} + 4\mathrm{H^+} + 4\mathrm{e^-}. \quad (1)$$

As shown in Figure 3a, j is determined by field-aided transport of mobile ions through the oxide layer under a constant potential U. The efficient electric field F_e across the oxide layer is:

$$F_\mathrm{e} = \frac{U}{\delta_\mathrm{b}}, \quad (2)$$

where δ_b is the thickness of the compact oxide layer. As j decreases continuously in stage I, δ_b increases constantly following the equation [49]:

$$\delta_\mathrm{b} = \frac{\beta U}{\ln\frac{j}{\alpha}}, \quad (3)$$

where α and β are the electrolyte and material dependent constants [49]. After Stage I, in order to maintain the oxidation process, ions (i.e. O^{2-}, OH^-, Ti^{4+}, F^-) must move quickly through the oxide layer and porosity is created due to F^- [19]:

$$\mathrm{TiO_2} + 6\mathrm{F^-} + 4\mathrm{H^+} \rightarrow [\mathrm{TiF_6}]^{2-} + 2\mathrm{H_2O}. \quad (4)$$

As a result, j rises in stage II. Similar to the case of oxide formation, oxide dissolution is also determined by field-aided F^- migration and therefore, the electric field F_d for F^- migration also decreases with increasing δ_b:

$$F_d = \frac{U}{\delta_b}. \tag{5}$$

Combining Eq. (3) with Eq. (5), the equation is obtained：

$$F_d = \frac{\ln\frac{j}{\alpha}}{\beta}. \tag{6}$$

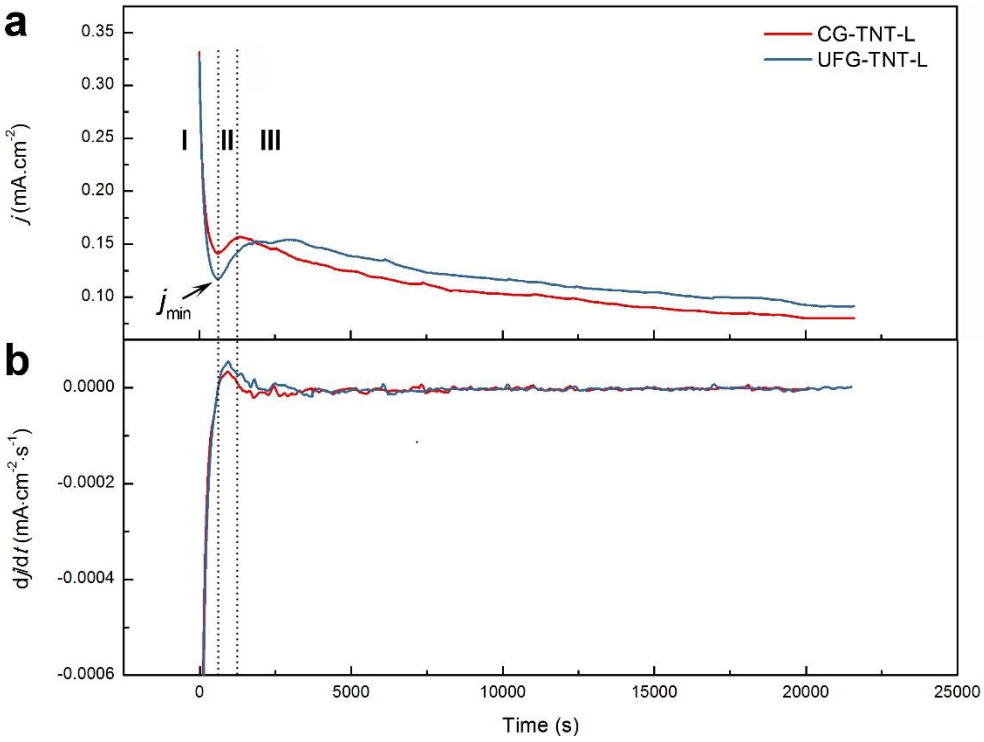

Figure 3. (a) Current density-time curves during anodization and (b) Corresponding time derivatives of the CG-TNT-L and UFG-TNT-L samples.

To further study the effects of grain size on the nucleation and growth of TNTs, high resolution measurements of the time derivative (dj/dt vs. time) are performed (Figure 3b). Although UFG-TNT-L and CG-TNT-L reach j_{min} almost at the same time, dj/dt exhibits no singularity or change of behavior for both samples at j_{min}, thus j_{min} cannot represent the

beginning of nucleation. Actually, dj/dt slows down before reaching j_{min}, indicating that nucleation of some early random nanopores occur on the surface of the compact TiO_2 even though δ_b is still on the rise. The CG-TNT-L and UFG-TNT-L samples show the same dj/dt curves in this stage, suggesting that nanotube nucleation is not affected by the grain size of substrate. The influence of the grain size on the growth of TNTs appears at j_{min} but it is lower on the UFG substrate (Figure 3a). There is a competition between electrochemical Ti oxidation (increasing δ_b) at the Ti/oxide interface and TiO_2 dissolution (decreasing δ_b) at the oxide/electrolyte interface and accordingly, j_{min} corresponds to the point when dissolution surpasses oxidation, at which the oxide thickness is the largest. Based on Eq. (6), F_d of UFG-TNT-L is less than that of CG-TNT-L corresponding to a thicker compact oxide layer and smaller migration rate of F^- ions.

3.4 Amorphous-anatase transformation of TNTs during annealing

Figure 4a shows the XRD patterns of different samples including the CG and UFG substrates, as-anodized CG-TNT-L and UFG-TNT-L samples, as well as annealed CG-TNT-L-A and UFG-TNT-L-A samples. Only the XRD results of the long TNTs are shown here as the short TNTs do not show any peaks from the oxide after annealing (Figure S1) probably because the crystal contents in the thin oxide layers are below the detection limit of XRD. Nevertheless, the TEM and SAED results shown in Figure S2 indicate the formation of crystals in the short TNTs after annealing. Even with the long TNTs, the layer can still be penetrated by the X-ray. The (100), (002), (101) and (102) planes are the main peaks of α titanium and no phase transformation of the titanium substrate occurs during anodization and subsequent annealing. For the CG substrate (Figure 4a, blue pattern),

only peaks of α titanium can be found. Compared to the XRD profile of the CG substrate, peak broadening is observed from the HPT substrate (Figure 4a, purple pattern) probably due to grain refinement and internal micro-strain [47]. The micro-strain $\langle \varepsilon^2 \rangle^{\frac{1}{2}}$ and crystal size *D* of the HPT substrate calculated by the Rietveld full peak refinement method are 0.19 % and 49 nm, respectively. As for the TNT layers, anodization and annealing change the crystallinity. In addition to the peaks arising from α titanium, a broad peak located at 25° - 34° is visible after anodizing the CG sample (Figure 4a, red pattern) but no other TiO_2 peaks can be found indicating that the as-anodized TNT layer is amorphous [50]. Similarly, the UFG-TNT-L sample (Figure 4a, black pattern) shows a broad peak at 25° - 34°, suggesting an amorphous nature.

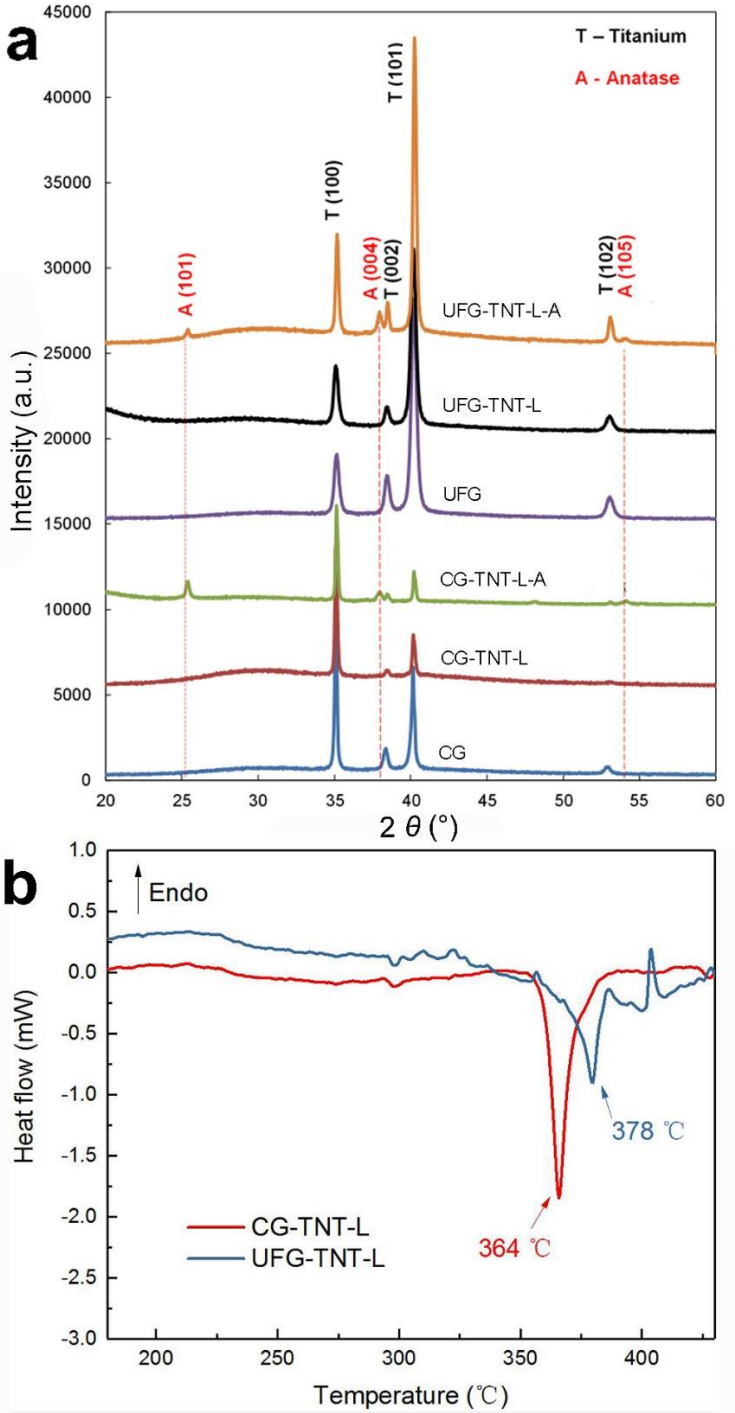

Figure 4. (a) XRD patterns of the CG and UFG samples before and after anodization as well as post-anodization annealing; (b) DSC results of the long TNT layers on the CG and UFG substrates.

After annealing, the CG-TNT-L-A and UFG-TNT-L-A samples show the (101), (004) and (105) peaks from anatase, demonstrating crystallization of amorphous titania. However, the relative peak intensities of the two annealed samples are different. For the CG-TNT-L-A sample (Figure 4a, green pattern), the strongest anatase peak is the (101) peak, whereas the (004) peak is the most intense peak in the UFG-TNT-L-A sample (Figure 4a, orange pattern). The crystallographic preferred orientation (CPO) defined in Eq. (7) can be utilized to semi-quantitatively measure the changes in the orientation of the (X) peak and (Y) peak [51], corresponding to (004) and (101) peaks in the present study. In the equation, I_X and I_Y refer to the intensity of the two peaks in the anatase phase, which can be compared to the ratio determined from a reference anatase sample (tetragonal, $I4_1/amd$, JCPDS 21-1272). The CPO values are calculated to be 0.71 and 0.93 for CG-TNT-L and UFG-TNT-L, respectively, indicating that the extent of preferred orientation for the annealed TNTs on the UFG substrate is higher than that on the CG substrate.

$$\mathrm{CPO}\ \frac{I^X}{I^Y} = \frac{\frac{I^X_{film}}{I^Y_{film}} - \frac{I^X_{ref}}{I^Y_{ref}}}{\frac{I^X_{film}}{I^Y_{film}}}. \tag{7}$$

XRD shows the texture difference of TNTs on the CG and UFG substrates after crystallization. To further study the influence of substrate grain-refinement on crystallization of amorphous TNTs, DSC experiments are conducted on the CG-TNT-L and UFG-TNT-L samples to determine the phase transformation of the as-anodized amorphous TNTs upon annealing. As shown in Figure 4b, phase transformation in both samples is evident. In particular, the main peak of CG-TNT-L sample in Figure 4b is an exothermic peak at 364 ˚C and it occurs at 378 ˚C for the UFG-TNT-L sample. These two peaks can be attributed to the transformation from the amorphous to anatase phases [52]. The

reported temperature of amorphous - anatase transformation is generally between 330 and 450 ºC [33,53] and in line with our results.

3.5 Chemical composition of TNTs

To study the influence of substrate grain size and annealing on the chemical composition of TNTs with different lengths, Figure 5 compares the XPS spectra of the Ti substrate and different TNT layers and the relative atomic ratios are presented in Table S2. The surface of the two substrates before anodization are mainly composed by Ti and O, whereas the high carbon content can be ascribed to carbon contamination. This is because titanium is very active and so a thin oxide layer forms readily upon air exposure. All the TNTs show titanium (Ti 2p), oxygen (O 1s), carbon (C 1s), fluoride (F 1s), as well as a small content of nitrogen (N 1s). The main impurities in the TNT layers are carbon and fluorides, and small N 1s peaks (400 eV) due to residual NH_4F-containing electrolyte are also detected.

The high-resolution XPS spectra of F 1s, O 1s and Ti 2p in Figures 5b, 5c and 5d are background-subtracted by the nonlinear iterative Shirley method [53]. All the curves marked by "A" refer to the annealed states. The F 1s peak (Figure 5b) primarily in the form of $[TiF_6]^{2-}$ at 684.9 eV quantifies the remaining fluorine in TNTs. Similar to the previous results [28,29], Figure 5b shows that annealing is efficient in reducing the F contents in the TNTs layers. After anodization, the long TNTs have smaller F contents than the short TNTs probably because the surface of the long TNTs is more distant to the $[TiF_6]^{2-}$ releasing sites at the bottom of the TNTs. After annealing at 350˚C for 1 h, F is almost eliminated from the short TNTs, but some residual F is still present on the long TNTs

(Figure 5b). It appears that the grain structure of the titanium substrate does not affect the F contents in the TNT layers.

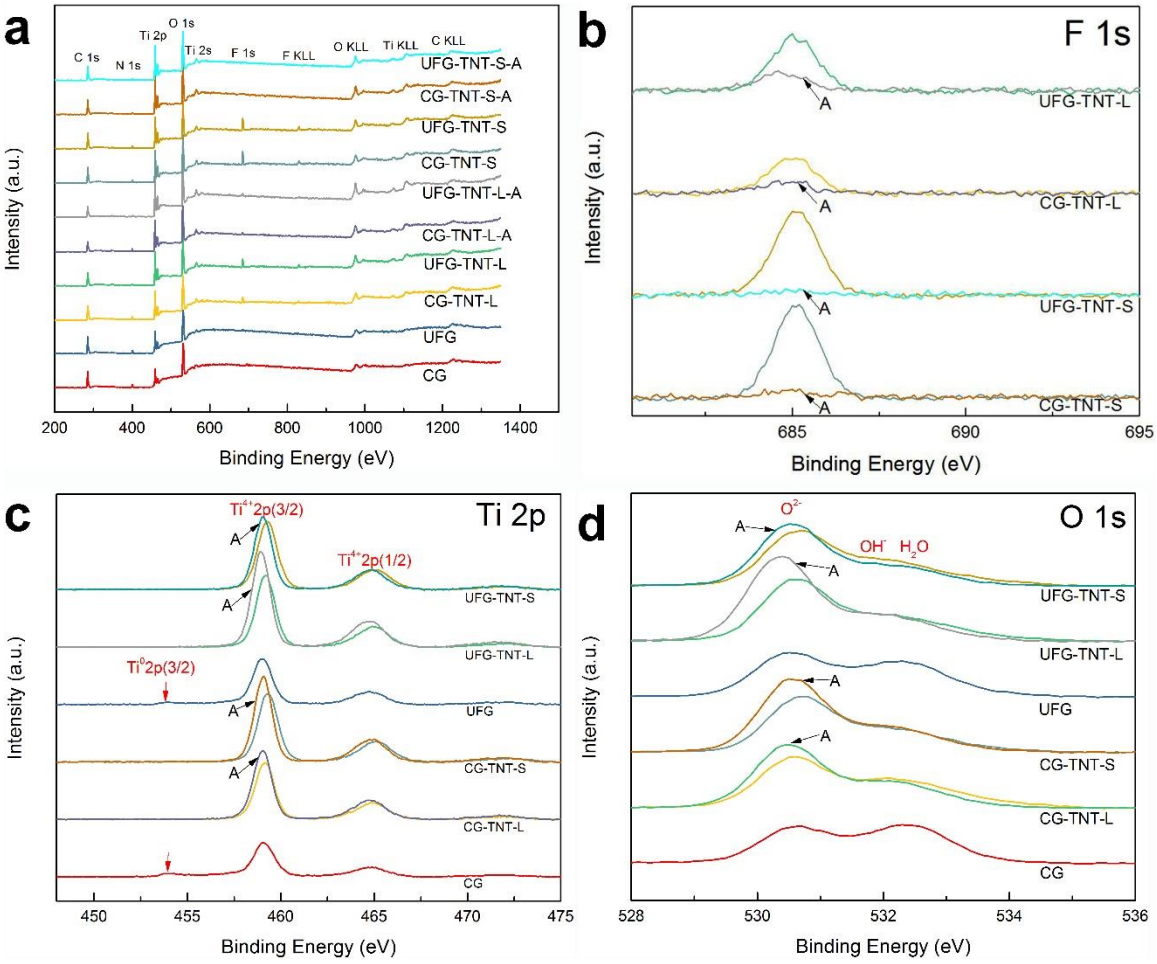

Figure 5. (a) Full survey XPS spectra, (b) High-resolution F 1s spectra, (c) High-resolution O 1s spectra, and (d) High-resolution Ti 2p spectra.

Formation of titanium oxides is confirmed by the peaks of Ti^{4+} 2p (3/2) and Ti^{4+} 2p (1/2) at 459.1 and 464.8 eV (Figure 5c), respectively, as well as O 1s peak at 530.4 eV (Figure 5d), which are the characteristics of Ti^{4+} and O^{2-} in TiO_2. The annealed TNTs show

more intense Ti^{4+} 2p (3/2) and Ti^{4+} 2p (1/2) peaks (Figure 5c). The Ti^{0} 2p (3/2) peak at 454.1 eV is related to metallic Ti, which is only detectable from the CG and UFG samples (indicated by the red arrows in Figure 5c). Disappearance of the Ti^{0} peak after construction of TNTs confirms the full coverage of surface TiO_2 (Figure S3). As shown in Figure 5d , the O 1s spectra show an intense O 1s peak corresponding to Ti−O bonding at 530.5 eV and another peak at a higher energy due to surface OH^- and H_2O species [54]. All the annealed TNTs show more intense O 1s peaks corresponding to O^{2-} in TiO_2 (Figure 5d).

3.6 Adhesion strength of TNTs

Figure 6 shows the SEM micrographs of the nanoscratch tracks of the TNT layers and the critical loads when initial spallation and continuous spallation of TNTs start to occur. The short TNTs (CG-TNT-S, UFG-TNT-S, CG-TNT-S-A and UFG-TNT-S-A) have better adhesion strength than the long ones (CG-TNT-L, UFG-TNT-L, CG-TNT-L-A and UFG-TNT-L-A) as adhesion failures marked by blue and red arrows occurs later on the short TNTs. Different with some previous reports [27,55–57], annealing has a negative effect on the adhesion strength of both the long and short TNT layers. Moreover, TNTs fabricated on the UFG substrates (UFG-TNT-S, UFG-TNT-S-A, UFG-TNT-L and UFG-TNT-L-A) possess better adhesion strength than those on the CG substrates (CG-TNT-S, CG-TNT-S-A, CG-TNT-L and CG-TNT-L-A), indicating that the HPT pre-treatment can enforce the binding between TNTs and titanium.

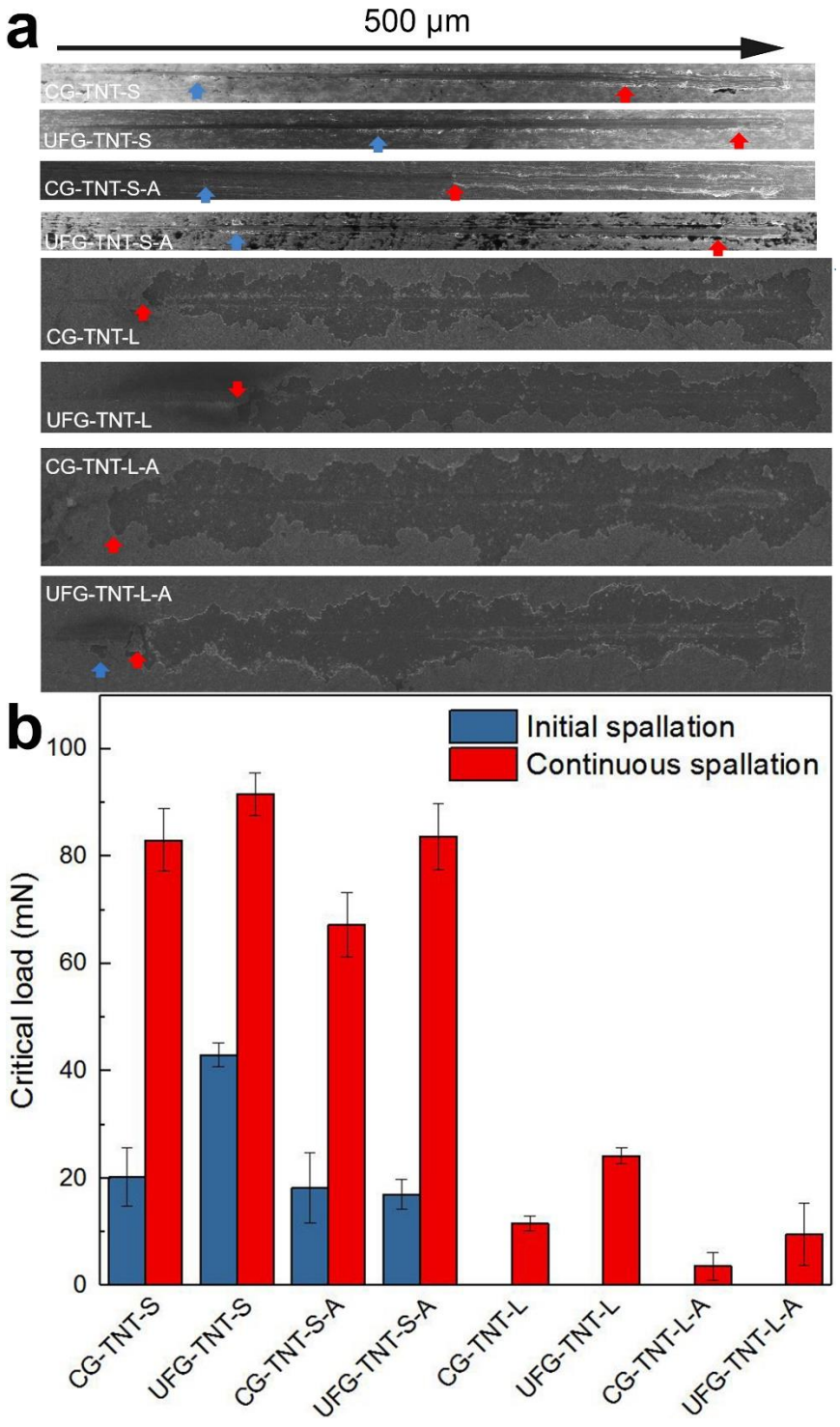

Figure 6. (a) SEM micrographs of the nanoscratch tracks on the TNT layers: where the blue arrows mark the sites of initial spallation and red arrows mark the sites of earliest continuous spallation; (b) Critical loads derived from the nanoscratch test.

3.7 Adhesion failure analysis

As shown in Figures 7a and 7b, the rear parts of the nanoscratch tracks are investigated to analyze the failure modes of the long and short TNTs. Although TNT-L and TNT-S fabricated on the CG substrate show different failure modes, the other long TNTs produced under different conditions show a similar failure mode as the short ones. As shown in Figure 6a and Figure 7a, the long TNTs exhibit flaking and gross spallation in front of the indenter at loads above the critical one in both the track and adjacent areas. Moreover, cracks can be found from the remaining adhering long TNTs, and possibly the internal stress leads to poor adhesion strength of the long TNTs. On the contrary, the short TNTs fabricated on the CG substrate have better adhesion strength than the long TNTs (Figure 6). Even at the end of nanoscratch test under a load of up to 100 mN, short TNTs do not show serious damage (Figure 7b) and the surrounding TNTs are intact without cracks. The magnified SEM image of the track on short TNTs is shown in Figure 7c, which reveals that the TNTs still adhere to the substrate after plastic deformation, although slight cohesive buckling or spallation can be observed at the edge of the track on short TNTs. The results indicate adhesion-related failures and spallations are due to elastic deformation [64]. The failure mode of short TNTs is similar to that of the TNTs on Ti-6Al-4V alloys previously reported [35]. A further analysis of the stress distribution in the TNT layers under indentation will be provided in Section 4.1.

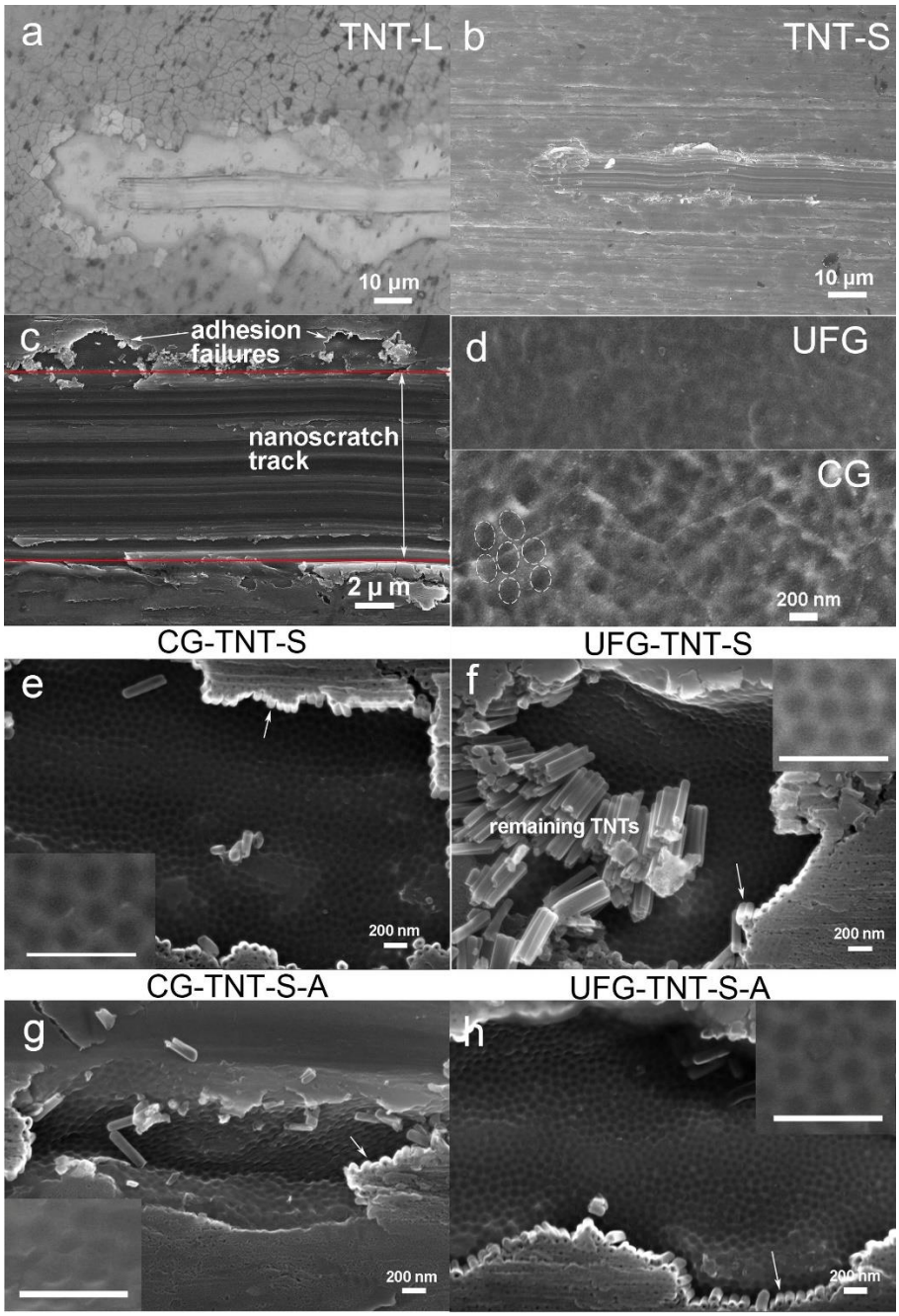

Figure 7. SEM micrographs of the end of the nanoscratch tracks: (a) TNT-L and (b) TNT-S on the CG substrate; (c) Typical adhesion failure of TNT-S at the edge of nanoscratch track; (d) CG and UFG substrates after removal of the TNT layers after one-step anodization; Failure sites show the TNTs/Ti interfaces on (e) CG-TNT-S, (f) UFG-TNT-S, (g) CG-TNT-S-A, and (h) UFG-TNT-S-A.

Before the second anodization step to produce the long TNTs, the UFG and CG Ti substrates are characterized by SEM after removing the TNT layers produced by the first step (Figure 7d). Grain boudaries can be identified from the CG substrate, suggesting different electrochemical reactivity of grain boudaries and grain interior during anodization. The dimples in the hexagonal arrangement are connected to the bottom of the nanotubes (highlighted with dotted lines). Only a few nanotubes stand on the grain boudaries while most of the TNTs are connected to the grain interior. In comparison, the UFG substrate does not show any grain boundaries under SEM observation (Figure 7d) because the grain size (138 nm, revealed by the TEM image in Figure 1b) is beyond the resolution of SEM. Since the grain size of the UFG substrate is approximately 1/239 of that of the CG substrate, most of the nanotubes are located at the grain boudaries of UFG subsrate.

As long TNTs have cracks throughout the layer (Figure 7a), only short ones are investigated to identify the influence of annealing and grain refinement on the adhesion strength. The interfaces (indicated by white arrows) between the short TNTs and substrates (CG-TNT-S, UFG-TNT-S, CG-TNT-S-A, and UFG-TNT-S-A) at the failure sites are shown in Figures 7e, 7f, 7g and 7h with the insets showing the haxagonal arrangment of substrate dimples. Adhesion failure occurs on the surface full of hexagnally aligned dimples which are closedly connected to the TNT bottoms. At the failure site on UFG-TNT-S (Figure 7f), some TNTs are loose but still adherent, corroesponding to the best adhesion of this sample. The chemical compostions of the TNTs/Ti interfaces are shown in Table 2 **错误!未找到引用源。**, which indicates that the annealed CG-TNT-S-A and UFG-TNT-S-A have smaller F concentrations than CG-TNT-S and UFG-TNT-S.

Table 2 Chemical compositions of the TNTs/Ti interfaces of short TNTs.

Element (at.%)	CG-TNT-S	UFG-TNT-S	CG-TNT-S-A	UFG-TNT-S-A
Ti	85.23 ± 1.15	95.91 ± 1.95	82.76 ± 2.01	88.10 ± 2.10
O	11.45 ± 0.75	2.04 ± 0.21	15.7 ± 0.84	10.25 ± 0.65
F	3.32 ± 0.25	2.05 ± 0.19	1.53 ± 0.17	1.64 ± 0.19

3.8 Biocompatibility of TNTs

To investigate the influence of TNTs/Ti adhesion strength on the adhesion and proliferation of HMSCs, CCK8 assays are conducted after incubating HMSCs on CG-TNT-S and UFG-TNT-S up to 72 h (Figure 8a). The TNTs on UFG-TNT-S show improved cell adhesion and proliferation after incubation for 24 and 72 h, but no significant difference in cell adhesion (6 h) is detected between these two groups. Up-regulation of ALP and OCN gene expression can also be observed from the UFG-TNT-S group after osteogenic culturing HMSCs for 14 days. Both samples support spreading of HMSCs with a polygonal shape and extended pseudopodia (Figures 8c and 8d). When loads of 0-100 mN (Figure 8e) and 0-30 mN (Figure 8f) are applied, the smaller elastic displacement on UFG-TNT-S at the beginning indicates that the short TNTs have a larger elastic modulus on the UFG substrate than those on the CG substrate. Based on the nanoscratch and wettability tests, the surface roughness values of CG-TNT-S and UFG-TNT-S are 41.4 ± 8.2 nm and 48.9 ± 14.1 nm and the corresponding water contact angles are 57° ± 2° and 55° ± 4°, respectively (Figure S4). There is no significant difference between the two groups.

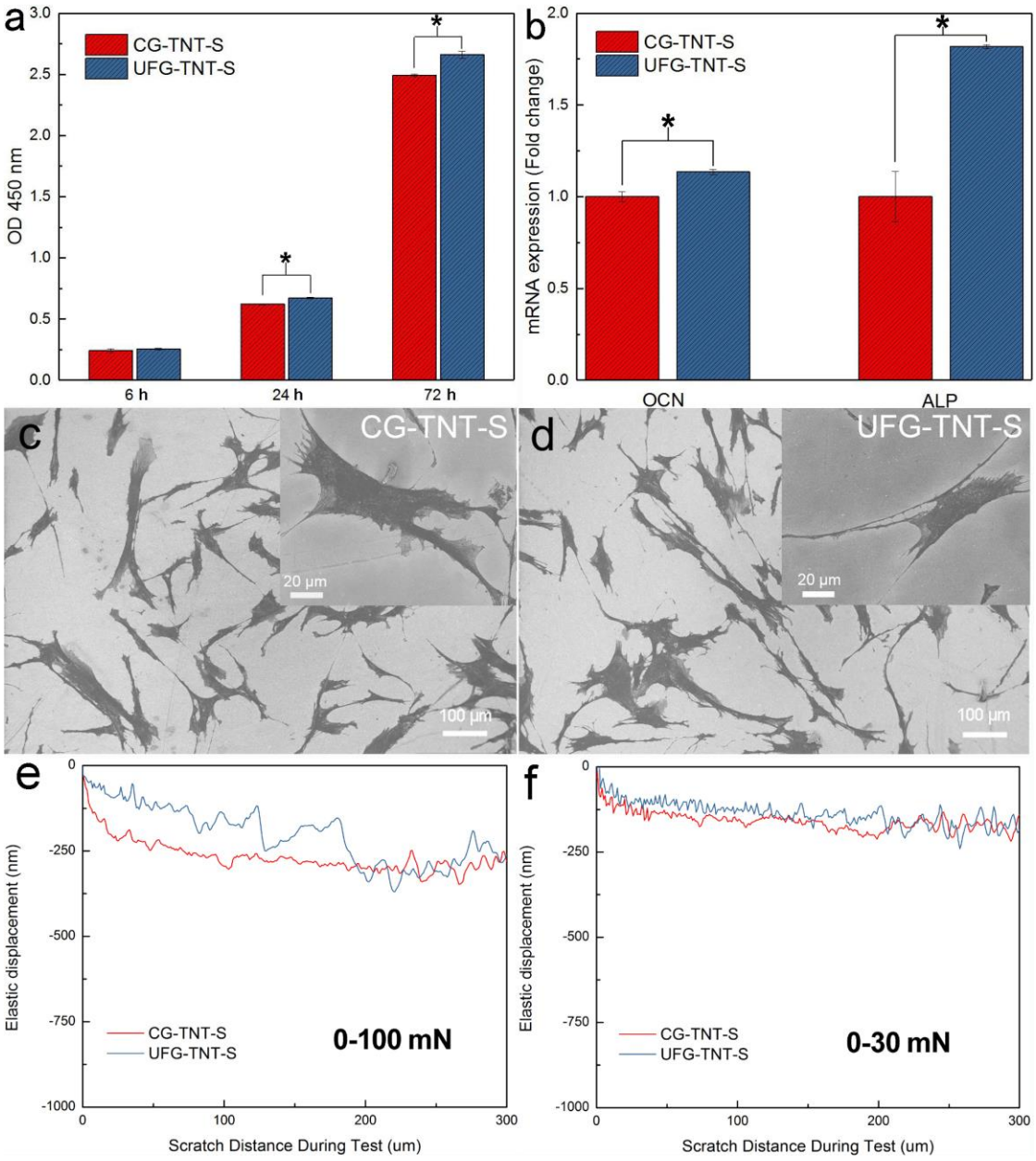

Figure 8. (a) Time-dependent viability of HMSCs cultured on CG-TNT-S and UFG-TNT-S; (b) Expression of osteogenesis-related genes (OCN and ALP) after culturing HMSCs on CG-TNT-S and UFG-TNT-S samples for 14 days with * denoting $p < 0.05$ compared with the CG-TNT-S group; SEM images of the HMSCs cultured on (c) CG-TNT-S and (d) UFG-TNT-S for 24 hours; Elastic displacement of CG-TNT-S and UFG-TNT-S under a load of (e) 0-100 mN and (f) 0-30 mN during the nanoscratch test.

4. Discussion

4.1 Failure modes of long and short TNTs

In the nanoscratch test, the type of failure depends on factors including the load, indenter geometry, coating thickness, residual stress in the coating, substrate hardness, as well as interfacial adhesion [35]. Generally, the critical load at which a failure is initiated (initial spallation) or occurs regularly along the track (continuous spallation) is used to assess the adhesion strength of the coating [58]. Therefore, a simple comparison between the long and short TNTs is invalid due to the different failure modes as discussed in Section 3.7. Nonetheless, the short TNTs have better adhesion qualitatively and quantitative evaluation of the influence of grain refinement and annealing on the adhesion strength of TNTs is still valid. The adhesion-related critical load based on initial and continuous spallation of TNTs is shown in Figure 6b. Figures 9a and 9b illustrate the side and front views of the cube corner indenter in contact with the TNTs/Ti system and the distribution of stress at different sites is also presented. As shown in Figure 9a, the TNTs in front of the indenter tip experience triaxial compressive stress, whereas the densified TNT layer under and behind the indenter experiences tensile stress along the indenter sliding direction. The triaxial compressive stress in front of the indenter is the main cause for full spallation of the long TNTs as shown in Figure 9c. However, the same stress in front of the indenter only leads to plastic deformation of short TNTs which adhere even after being crushed (Figure 7b). The occasional spallation of short TNTs along the edge of the track (Figure 9d) stems from elastic deformation of the coating and substrate during elastic recovery [64].

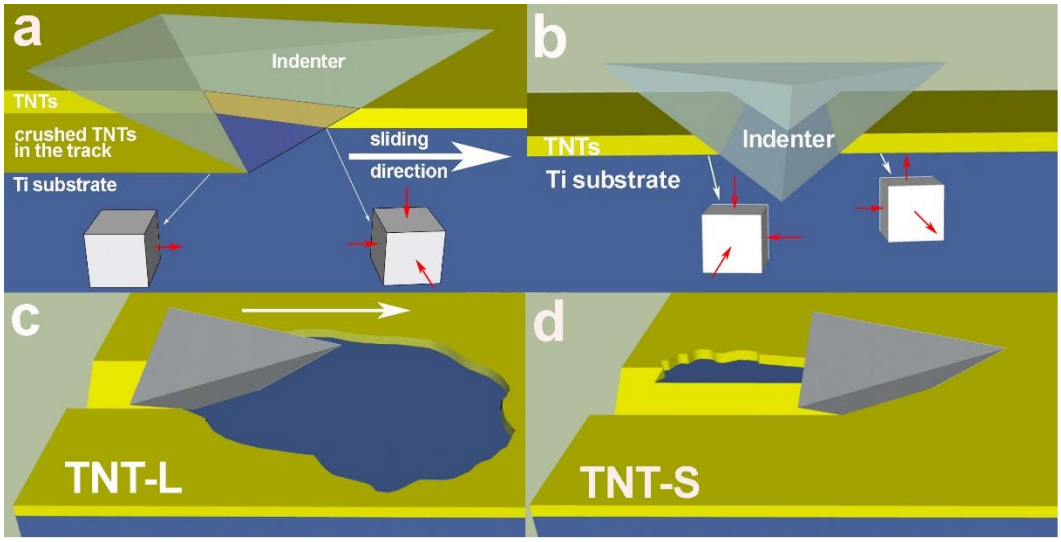

Figure 9. Stress distribution at the TNTs/Ti interface: (a) Side view and (b) Front view of the cube corner indenter during the nanoscratch test; Schematic illustration of the adhesion failure modes of (c) TNT-L and (d) TNT-S.

4.2 Influence of anodization on the TNTs/Ti adhesion strength

To identify the weakest point of attachment between the TNTs and Ti substrate as well as the structure of TNTs/Ti interface, Figure 10 presents schematics according to the adhesion failure sites shown in Figure 7. A native oxide film with a thickness of 3-7 nm forms on pure titanium at room temperature (Figure 10a) [59] and from the TiO_2 film to the bulk metal, the O/Ti ratio decreases gradually from 2 to 1 at the TiO_2\Ti interface [59]. Hydroxide and chemisorbed water bind to Ti cations on the surface and the properties depend on the fabrication conditions and processing history [60]. The structure of TiO_2\Ti interface of pure Ti is shown in Figure 10d [60] and adhesion is mainly provided by chemical Ti-O bonding.

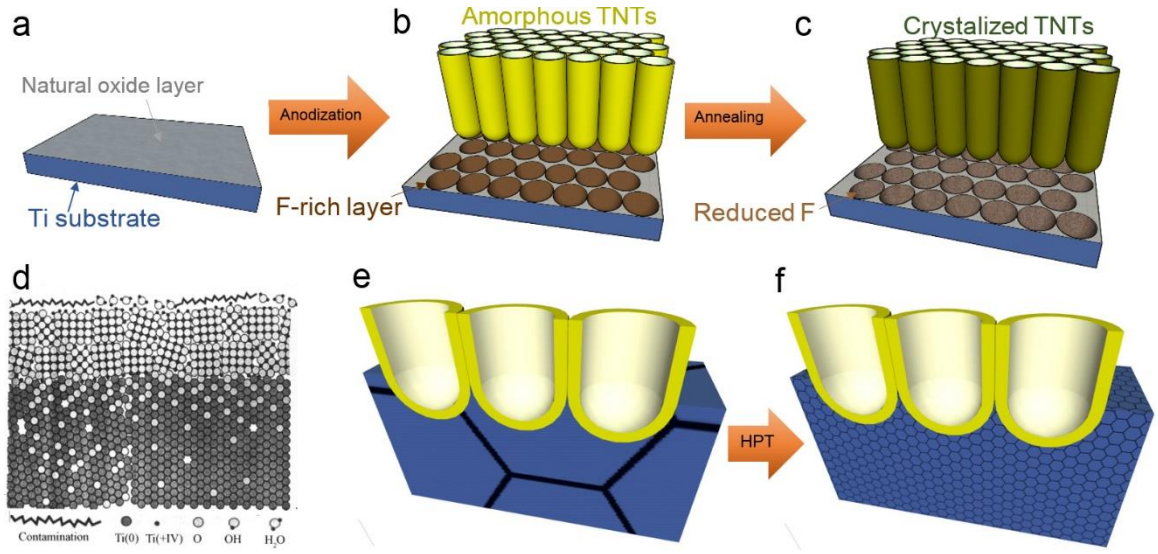

Figure 10. Schematics of the Ti surface after anodization and annealing: (a) Ti substrate with a surface native oxide layer, (b) Amorphous TNTs on Ti after anodization, and (c) Crystallized TNTs on Ti after annealing; Interfaces of (d) Surface native oxide film on pure titanium [60], (e) TNTs on the CG substrate, and (f) TNTs on the UFG substrate.

During anodization, the surface native oxide on pure titanium is converted into a hexagonally-aligned TiO_2 nanotube layer [1] as shown in Figure 10b. Except the Ti-O bonding at interface, the contact area between the TNTs and substrate increases due to the formation of hexagonally-arranged dimples (Figures 7e, 7f, 7g and 7h). However, the interface is F rich (Table 2) as previously reported [19–21] and a considerable amount of internal stress exists due to the volume expansion of transforming compact TiO_2 layers into nanotubular layers [24,25]. Adhesion weakens as the length of TNTs increases (Figure 6b). As shown in Figure 7a, cracks occur on the surface of long TNTs and similar cracked surfaces have been previously reported [33,61]. In this respect, reduction of TNTs length is an effective way to decrease the inherent internal stresses and improve the adhesion

strength [12]. According to Figure 3a, 1 h is the time point when formation of TNTs becomes steady (stage III) in which the nanotubular structure can be produced with minimum internal stress. The weakest spots that failures often occur are the boundaries between the TNTs which also contain F ions (Table 2) [3,19]. Therefore, maybe it is desirable to reduce the F contents at these boundaries to improve adhesion strength by post-anodization annealing. However, based on the opposite results shown in Figure 6, further investigation about the influence of annealing on the microstructure and morphology of TNTs is required.

4.3 Influence of annealing on TNTs/Ti adhesion strength

Annealing has been shown to strengthen adhesion [27]. For example, increased Ti-O bonding has been reported after annealing [27] due to the formation of a thin compact oxide layer at the interface [55]. The XPS results in Figure 5 confirm the increased Ti-O bonding after annealing in conjunction with reduction in the F contents. Therefore, the decrease in the adhesion strength may be related to the crystallization process (Figure 10c). The phase transformation of amorphous TNTs into crystallized (anatase or rutile) TNTs has been previously reported [1,3,8,31,32,62]. In this study, amorphous TNTs are converted into anatase without forming other polymorphs of TiO_2 (Figure 4a). In the meantime, the overall morphology of TNTs does not change (Figure 2) after *in situ* solid-state phase transformation from the amorphous to anatase phases [29]. There have been reports about annealing TNTs at 450 ˚C [29,61], but from the perspective of mechanical stability, annealing at 450 ˚C can produce structural damage of anodic TiO_2 nanotubes even if the heating rate is reduced to 0.1 ˚C/s [55]. The TNTs annealed at 350 ˚C do not show structural

defects [55] and so this temperature is chosen in our study. However, local microstructural changes such as pits formation at the bottom of TNTs (Figures 2g, 2h, 2o, and 2p) still occur after 350 ˚C annealing, which may reduce the contact area between the TNTs and substrate resulting in decreased adhesion strength.

The reason for the formation of bottom pits are not clear but it may be related to crystallization. It has been reported that the transformation from nanocrystalline anatase to rutile is governed by interface nucleation or surface nucleation [63], and the phase transformation of TiO_2 from the amorphous state to crystalline state may be influenced by a similar mechanism [64]. Generally, nucleation of nanocrystals in the amorphous TiO_2 layer takes place at the TiO_2\Ti interface [65] because the activation energy of interface nucleation is the lowest. Crystallization of TiO_2 is accompanied by the shrinkage of TiO_2 nanotubes [55] as the volume expansion diminishes from 2.40 to 1.76 when amorphous titania morphs into anatase [24]. The initiation sites for crystallization shrink most severely and pits are formed at the interface. Furthermore, nanoscale bubbles are developed by local generation of oxygen [65] and fluorine gas and this is another possible reason for the formation of cavities at the TNTs/Ti interfaces.

4.4 Influence of substrate grain refinement on the phase transformation of amorphous TNTs

HPT processing changes the grain size and dislocation density of CP Ti and these microstructural features also affect the anodization behavior of Ti [41]. During the HPT processing, the equivalent strain, ε_h, increases with rotations [42] whereas the CG sample has no strain imposed on it, i.e. $\varepsilon_h = 0$. After ten HPT rotations, the microstructure is

homogeneous with the grain size down to about 138 nm (Figure 1c). The Ti sample processed by HPT shows large grain boundary misorientation angles when ε_h exceeds 3.7 [66], which is confirmed by SAED that a large number of well-spaced spots have the circular arrangement (Figure 1c inset, $\varepsilon_h \approx 6$). The grain boundaries in the HPT sample are curved and wavy, which are the characteristics of non-equilibrium grain boundaries [67]. The heterogeneous contrast of grain interiors is caused by defects such as dislocations and clusters of dislocations [67].

As shown by the XRD patterns in Figure 4, the peaks from the UFG substrate (purple patterns) broaden compared to those from the CG substrate (blue patterns), confirming substantial grain refinement and increased micro-strain after HPT processing. The dislocation density ρ can be calculated from the lattice micro-strain $\langle \varepsilon^2 \rangle^{\frac{1}{2}}$ and the crystallite size D derived from XRD patterns [68]:

$$\rho = \frac{2\sqrt{3}\langle \varepsilon^2 \rangle^{\frac{1}{2}}}{Db}, \tag{9}$$

where b is the Burgers vector. With increasing HPT deformation, the crystallite size D decreases and micro-strain $\langle \varepsilon^2 \rangle^{\frac{1}{2}}$ increases and hence, the dislocation density ρ increases. In addition, the significant spreading of spots in the SAED image (Figure 1c inset) confirms the high micro-strain [47]. The dislocation density is calculated from the crystallite size and micro-strain derived from Figure 3 and has a value as high as 4.6×10^{14} m^{-2} for the HPT-processed sample.

There have been several reports describing the effects of substrates on nanotubular TiO_2 layers including the influence of orientation [69], polishing techniques [70], surface roughness [71], and grain sizes [69, 70]. Our results show that HPT processing of Ti

substrates produces longer and more homogeneous TNTs (Figure 2c) because the larger density of grain boundaries and dislocations facilitate consumption of Ti and growth of TNTs by releasing additional energy. The XRD and DSC analyses of different TNTs corroborate the influence of substrate grain refinement on the phase transformation of amorphous TNTs. After annealing at 350 ˚C for 1 h, the only crystalline phase in the TNT layer is anatase, in which the dominant peak at 25.3° is generally from the (101) plane [7] such as CG-TNT-L-A (Figure 4a, green pattern). This is because the (101) facet is thermodynamically stable on account of the relatively small surface energy (0.44 $J \cdot m^{-2}$) [73]. However, both experimental and theoretical studies have shown that the (001) facet of anatase titanium dioxide with a surface energy of 0.90 $J \cdot m^{-2}$ is more reactive than the (101) facet [74]. The dominant (004) peak of UFG-TNT-L-A implies that the perpendicular TNTs are preferentially oriented along the [001] direction of the TiO_2 anatase structure. Although the mechanism of the (001)-oriented TNTs fabricated on the UFG sample is not fully clear, the grain size and dislocations of the substrate seem to play important roles.

The TNTs/Ti interface is crucial to the dynamics of TNTs crystallization. For instance, when the TNTs are attached to the underlying Ti substrate, initiation of the anatase-rutile phase transformation starts at 500 °C compared to 600 °C for the detached TNTs [8]. DSC analysis shows that the crystallization temperature of amorphous TNT layer on the UFG substrate is higher than that of amorphous TNTs on the CG substrate (Figure 4b), suggesting that crystallization of amorphous TNT layers on the UFG substrate requires more energy. It is consistent with the XRD results that crystallized TNT layer on the UFG substrate contains more thermodynamically unstable (001) facets (Figure 4a). The phase stability and phase transformation kinetics in nanoscale solids are substantially different

from those in the bulk materials. An inversion of phase stability may take place as a result of the differentiation of internal and surface energies between the transformed polymorphs [75]. Typically, the stable phase of bulk TiO_2 is rutile but the less thermodynamically stable anatase phase can be obtained first by thermal treatment of amorphous TNTs and transformed into rutile at a higher temperature [8,31,32,62]. To investigate why a larger dislocation density at the TNTs/Ti interface delays crystallization of UFG-TNT-L, it should be noted that the crystallization of amorphous titania is activated by fluctuations of the structurally related precursor phases in the amorphous phase [64,76]. Since the UFG sample contains many more defects such as dislocations, grain boundaries, and vacancies than the CG sample, the amorphous oxide on the former has a higher free energy causing transformation into the anatase phase with a minority (001) plane during annealing. Similarly, the amorphous-anatase phase transformation of nanosized TiO_2 is retarded compared to the bulk sample [75].

4.5 Influence of grain refinement on TNTs/Ti adhesion strength and biocompatibility

As shown in Figure 7d, grain boundaries are revealed in the CG substrate after anodization because grain boundaries are more prone to etching. Therefore, grain boundaries can increase the contact areas at TiO_2\Ti interface [77,78], providing more mechanical anchorage to the surface oxide layer than the grain interior. Figure 7d shows that most of TNT bottoms are located at the grain interior of the CG substrate. With regard to the UFG sample, TNTs at the grain boundaries significantly increase and hence better adhesion strength is achieved (Figure 6b).

Grain refinement also affects the growth rate and chemical dissolution rate of TNTs (Figure 3a). The closed and dome-like bottoms separate the TNTs from the Ti substrate with the barrier layer δ_b, as shown in Eq. (3). At the same potential, a smaller j_{min} indicates a higher δ_b of TNTs on the UFG sample, corresponding to a smaller expansion factor [25] and lower internal stress than that of TNTs on the CG substrate. Moreover, the UFG-TNT-L sample has smaller F_d as discussed in Section 3.3, corresponding to smaller F^- migration rates. The EDS results in Table 2 further confirm that the F contents at the TNTs/Ti interfaces of UFG-TNT-S is less than that at the TNTs/Ti interfaces of CG-TNT-S, which consequently alleviate the adverse influence of the F-rich layer during anodization.

The UFG surfaces can mediate the behaviors of cells [79,80] and it has been reported that HMSCs are influenced by multiple biophysical factors such as the substrate topography, stiffness, as well as extrinsic mechanical cues including the strain, fluid flow, compression, and hydrostatic pressure [39]. In response to these mechanical properties, HMSCs can generate contractile forces and receive mechanical information that directs cellular functions [39]. The differentiation of HMSCs is related to the substrate stiffness and cells cultured on a stiffer substrate tend to be more osteogenic [81]. Therefore, the enhanced biocompatibility and osteogenic differentiation (Figures 8a and 8b) of HMSCs cultured on the UFG-TNT-S sample may be related to the larger elastic modulus, as indicated by the smaller elastic displacement during the nanoscratch test (Figures 8e and 8f).

5. Conclusion

In this study, HPT processing is employed to obtain UFG microstructure in Ti, on which

the adhesion of TNTs to the underlying Ti substrate is enhanced. The TNTs/Ti interface is systematically studied for better understanding the underlying mechanism for adhesion. A larger amount of grain boundaries at the interface provide more mechanical anchorage for adhesion, leading to preferentially oriented minority (001) facet in crystallized anatase phase after annealing the amorphous TNTs. Reducing the length of TNTs from 2.0 to 0.4 μm improves adhesion as the internal stress at the interface is reduced. Annealing of amorphous TNTs undermines the adhesion strength because cavities form at the interface during crystallization, although annealing is efficient in reducing the F concentrations in the TNTs layers. HPT processing can even enhance the elastic modulus of TNTs, further improving the biocompatibility and osteogenic differentiation of HMSCs.

Author information

Corresponding Authors

*E-mail: lp.tong@siat.ac.cn (Liping Tong)

*E-mail: paul.chu@cityu.edu.hk (Paul K. Chu)

*E-mail: hy.wang1@siat.ac.cn (Huaiyu Wang)

Acknowledgements

The authors acknowledge financial support from the National Natural Science Foundation of China (No. 31922040), Shenzhen Science and Technology Research Funding (Nos. SGLH20180625144002074 and JCYJ20180507182637685), Youth

Innovation Promotion Association of Chinese Academy of Sciences (No. 2017416), Leading Talents of Guangdong Province Program (No. 00201520), Shenzhen Peacock Program (No. KQTD2016030111500545), Science and Technology Service Network Initiative of Chinese Academy of Sciences (No. KFJ-STS-QYZX-035), China Postdoctoral Science Foundation (Nos. 2017LH039 and 2018M633184), Hong Kong Research Grants Council (RGC) General Research Funds (GRF) (No. CityU 11205617), as well as City University of Hong Kong Strategic Research Grant (SRG) (No. 7005264).

References

[1] P. Roy, S. Berger, P. Schmuki, TiO_2 Nanotubes: Synthesis and Applications, Angew. Chemie-International Ed. 50 (2011) 2904–2939. https://doi.org/10.1002/anie.201001374.

[2] G.K. Mor, O.K. Varghese, M. Paulose, K. Shankar, C.A. Grimes, A review on highly ordered, vertically oriented TiO_2 nanotube arrays: Fabrication, material properties, and solar energy applications, Sol. Energy Mater. Sol. Cells. 90 (2006) 2011–2075. https://doi.org/https://doi.org/10.1016/j.solmat.2006.04.007.

[3] D. Regonini, C.R. Bowen, A. Jaroenworaluck, R. Stevens, A review of growth mechanism, structure and crystallinity of anodized TiO_2 nanotubes, Mater. Sci. Eng. R Reports. 74 (2013) 377–406. https://doi.org/10.1016/J.MSER.2013.10.001.

[4] H. Nuhn, C.E. Blanco, T.A. Desai, Nanoengineered Stent Surface to Reduce In-Stent Restenosis in Vivo, ACS Appl. Mater. Interfaces. 9 (2017) 19677–19686. https://doi.org/10.1021/acsami.7b04626.

[5] N.K. Awad, S.L. Edwards, Y.S. Morsi, A review of TiO_2 NTs on Ti metal: Electrochemical synthesis, functionalization and potential use as bone implants, Mater. Sci. Eng. C. 76 (2017) 1401–1412. https://doi.org/https://doi.org/10.1016/j.msec.2017.02.150.

[6] T. Yu, H. Yin, Y. Zhou, Y. Wang, H. Zhu, D. Wang, Electrochemical Preparation of Porous Ti–13Zr–13Nb Alloy and Its Corrosion Behavior in Ringers Solution, Mater. Trans. 58 (2017) 326–330. https://doi.org/10.2320/matertrans.MK201627.

[7] M.H. Jung, M.J. Chu, M.G. Kang, TiO_2 nanotube fabrication with highly exposed (001) facets for enhanced conversion efficiency of solar cells, Chem. Commun. 48

(2012) 5016. https://doi.org/10.1039/c2cc31047c.

[8] K. Zhu, N.R. Neale, A.F. Halverson, J.Y. Kim, A.J. Frank, Effects of annealing temperature on the charge-collection and light-harvesting properties of TiO_2 nanotube-based dye-sensitized solar cells, J. Phys. Chem. C. 114 (2010) 13433–13441. https://doi.org/10.1021/jp102137x.

[9] R. Kupcik, P. Rehulka, Z. Bilkova, H. Sopha, J.M. Macak, New Interface for Purification of Proteins: One-Dimensional TiO_2 Nanotubes Decorated by Fe_3O_4 Nanoparticles, ACS Appl. Mater. Interfaces. 9 (2017) 28233–28242. https://doi.org/10.1021/acsami.7b08445.

[10] S. Ozkan, N.T. Nguyen, I. Hwang, A. Mazare, P. Schmuki, Highly Conducting Spaced TiO_2 Nanotubes Enable Defined Conformal Coating with Nanocrystalline Nb_2O_5 and High Performance Supercapacitor Applications, Small. 13 (2017) 1603821. https://doi.org/10.1002/smll.201603821.

[11] S. Cao, W. Huang, L. Wu, M. Tian, Y. Song, On the Interfacial Adhesion between TiO_2 Nanotube Array Layer and Ti Substrate, Langmuir. 34 (2018) 13888–13896. https://doi.org/10.1021/acs.langmuir.8b03408.

[12] M. Weszl, K.L. Tóth, I. Kientzl, P. Nagy, D. Pammer, L. Pelyhe, N.E. Vrana, D. Scharnweber, C. Wolf-Brandstetter, Á. Joób F., E. Bognár, Investigation of the mechanical and chemical characteristics of nanotubular and nano-pitted anodic films on grade 2 titanium dental implant materials, Mater. Sci. Eng. C. 78 (2017) 69–78. https://doi.org/10.1016/J.MSEC.2017.04.032.

[13] D. Wang, T. Hu, L. Hu, B. Yu, Y. Xia, F. Zhou, W. Liu, Microstructured Arrays of TiO_2 Nanotubes for Improved Photo-Electrocatalysis and Mechanical Stability,

Adv. Funct. Mater. 19 (2009) 1930–1938. https://doi.org/10.1002/adfm.200801703.

[14] S.P. Albu, A. Ghicov, S. Aldabergenova, P. Drechsel, D. LeClere, G.E. Thompson, J.M. Macak, P. Schmuki, Formation of Double-Walled TiO_2 Nanotubes and Robust Anatase Membranes, Adv. Mater. 20 (2008) 4135–4139. https://doi.org/10.1002/adma.200801189.

[15] J. Proost, J.F. Vanhumbeeck, Q. Van Overmeere, Instability of anodically formed TiO_2 layers (revisited), Electrochim. Acta. 55 (2009) 350–357. https://doi.org/10.1016/J.ELECTACTA.2008.12.008.

[16] J.C. Nelson, R.A. Oriani, Stress generation during anodic oxidation of titanium and aluminum, Corros. Sci. 34 (1993) 307–326. https://doi.org/10.1016/0010-938X(93)90009-6.

[17] T. Li, K. Gulati, N. Wang, Z. Zhang, S. Ivanovski, Understanding and augmenting the stability of therapeutic nanotubes on anodized titanium implants, Mater. Sci. Eng. C. 88 (2018) 182–195. https://doi.org/10.1016/J.MSEC.2018.03.007.

[18] R. Narayanan, T.-Y. Kwon, K.-H. Kim, TiO_2 nanotubes from stirred glycerol/NH_4F electrolyte: Roughness, wetting behavior and adhesion for implant applications, Mater. Chem. Phys. 117 (2009) 460–464. https://doi.org/10.1016/J.MATCHEMPHYS.2009.06.023.

[19] J.M. Macak, H. Tsuchiya, A. Ghicov, K. Yasuda, R. Hahn, S. Bauer, P. Schmuki, TiO_2 nanotubes: Self-organized electrochemical formation, properties and applications, Curr. Opin. Solid State Mater. Sci. 11 (2007) 3–18. https://doi.org/10.1016/J.COSSMS.2007.08.004.

[20] H. Habazaki, K. Fushimi, K. Shimizu, P. Skeldon, G.E. Thompson, Fast migration of fluoride ions in growing anodic titanium oxide, Electrochem. Commun. 9 (2007) 1222–1227. https://doi.org/10.1016/J.ELECOM.2006.12.023.

[21] Y. Zhang, Y. Han, L. Zhang, Interfacial structure of the firmly adhered TiO_2 nanotube films to titanium fabricated by a modified anodization, Thin Solid Films. 583 (2015) 151–157. https://doi.org/10.1016/J.TSF.2015.03.060.

[22] K. Lee, A. Mazare, P. Schmuki, One-Dimensional Titanium Dioxide Nanomaterials: Nanotubes, Chem. Rev. 114 (2014) 9385–9454. https://doi.org/10.1021/cr500061m.

[23] S. Berger, J. Kunze, P. Schmuki, D. LeClere, A.T. Valota, P. Skeldon, G.E. Thompson, A lithographic approach to determine volume expansion factors during anodization: Using the example of initiation and growth of TiO_2-nanotubes, Electrochim. Acta. 54 (2009) 5942–5948. https://doi.org/http://dx.doi.org/10.1016/j.electacta.2009.05.064.

[24] S.P. Albu, P. Schmuki, Influence of anodization parameters on the expansion factor of TiO_2 nanotubes, Electrochim. Acta. 91 (2013) 90–95. https://doi.org/10.1016/J.ELECTACTA.2012.12.094.

[25] A. Valota, D.J. LeClere, P. Skeldon, M. Curioni, T. Hashimoto, S. Berger, J. Kunze, P. Schmuki, G.E. Thompson, Influence of water content on nanotubular anodic titania formed in fluoride/glycerol electrolytes, Electrochim. Acta. 54 (2009) 4321–4327. https://doi.org/10.1016/J.ELECTACTA.2009.02.098.

[26] C. Prakash, M.S. Uddin, Surface modification of β-phase Ti implant by hydroaxyapatite mixed electric discharge machining to enhance the corrosion

resistance and in-vitro bioactivity, Surf. Coatings Technol. 326 (2017) 134–145. https://doi.org/10.1016/J.SURFCOAT.2017.07.040.

[27] J. Xiong, X. Wang, Y. Li, P.D. Hodgson, Interfacial Chemistry and Adhesion between Titanium Dioxide Nanotube Layers and Titanium Substrates, J. Phys. Chem. C. 115 (2011) 4768–4772. https://doi.org/10.1021/jp111651d.

[28] J.M. Macak, S. Aldabergerova, A. Ghicov, P. Schmuki, Smooth anodic TiO_2 nanotubes: annealing and structure, Phys. Status Solidi. 203 (2006) R67–R69. https://doi.org/10.1002/pssa.200622214.

[29] J. Yu, G. Dai, B. Cheng, Effect of Crystallization Methods on Morphology and Photocatalytic Activity of Anodized TiO_2 Nanotube Array Films, J. Phys. Chem. C. 114 (2010) 19378–19385. https://doi.org/10.1021/jp106324x.

[30] S. Cao, W. Huang, S. Zhang, L. Wu, Y. Song, A simple strategy to increase the interfacial adhesion between TiO_2 nanotube layer and Ti substrate, J. Alloys Compd. 772 (2019) 173–177. https://doi.org/10.1016/J.JALLCOM.2018.09.028.

[31] Y. Yang, X. Wang, L. Li, Crystallization and Phase Transition of Titanium Oxide Nanotube Arrays, J. Am. Ceram. Soc. 91 (2008) 632–635. https://doi.org/10.1111/j.1551-2916.2007.02133.x.

[32] K. Shankar, G.K. Mor, H.E. Prakasam, S. Yoriya, M. Paulose, O.K. Varghese, C.A. Grimes, Highly-ordered TiO_2 nanotube arrays up to 220 μm in length: use in water photoelectrolysis and dye-sensitized solar cells, Nanotechnology. 18 (2007) 65707. https://doi.org/10.1088/0957-4484/18/6/065707.

[33] H.J. Oh, S. Lee, B. Lee, Y. Jeong, C.-S. Chi, Surface characteristics and phase transformation of highly ordered TiO_2 nanotubes, Met. Mater. Int. 17 (2011) 613–

616. https://doi.org/10.1007/s12540-011-0813-9.

[34] J. Park, S. Bauer, P. Schmuki, K. von der Mark, Narrow Window in Nanoscale Dependent Activation of Endothelial Cell Growth and Differentiation on TiO_2 Nanotube Surfaces, Nano Lett. 9 (2009) 3157–3164. https://doi.org/10.1021/nl9013502.

[35] N. Hu, T. Hu, A. Gao, N. Gao, M.J. Starink, Y. Chen, W. Sun, Q. Liao, L. Tong, X. Xu, P.K. Chu, H. Wang, Homogeneous Anodic TiO_2 Nanotube Layers on Ti–6Al–4V Alloy with Improved Adhesion Strength and Corrosion Resistance, Adv. Mater. Interfaces. 6 (2019) 1801964. https://doi.org/10.1002/admi.201801964.

[36] R.Z. Valiev, Y. Estrin, Z. Horita, T.G. Langdon, M.J. Zehetbauer, Y.T. Zhu, Producing bulk ultrafine-grained materials by severe plastic deformation, Jom. 58 (2006) 33–39. https://doi.org/10.1007/s11837-006-0213-7.

[37] M.J. Starink, X. Cheng, S. Yang, Hardening of pure metals by high-pressure torsion: A physically based model employing volume-averaged defect evolutions, Acta Mater. 61 (2013) 183–192. https://doi.org/https://doi.org/10.1016/j.actamat.2012.09.048.

[38] M.J. Starink, X.G. Qiao, J. Zhang, N. Gao, Predicting grain refinement by cold severe plastic deformation in alloys using volume averaged dislocation generation, Acta Mater. 57 (2009) 5796–5811. https://doi.org/https://doi.org/10.1016/j.actamat.2009.08.006.

[39] J. Hao, Y. Zhang, D. Jing, Y. Shen, G. Tang, S. Huang, Z. Zhao, Mechanobiology of mesenchymal stem cells: Perspective into mechanical induction of MSC fate, Acta Biomater. 20 (2015) 1–9. https://doi.org/10.1016/j.actbio.2015.04.008.

[40] D.E. Ingber, Tensegrity-based mechanosensing from macro to micro, Prog. Biophys. Mol. Biol. 97 (2008) 163–179. https://doi.org/10.1016/j.pbiomolbio.2008.02.005.

[41] N. Hu, N. Gao, Y. Chen, M.J. Starink, Achieving homogeneous anodic TiO_2 nanotube layers through grain refinement of the titanium substrate, Mater. Des. 110 (2016) 346–353. https://doi.org/10.1016/j.matdes.2016.07.144.

[42] A.P. Zhilyaev, T.G. Langdon, Using high-pressure torsion for metal processing: Fundamentals and applications, Prog. Mater. Sci. 53 (2008) 893–979. https://doi.org/http://dx.doi.org/10.1016/j.pmatsci.2008.03.002.

[43] Y. Chen, N. Gao, G. Sha, S.P. Ringer, M.J. Starink, Microstructural evolution, strengthening and thermal stability of an ultrafine-grained Al–Cu–Mg alloy, Acta Mater. 109 (2016) 202–212. https://doi.org/10.1016/J.ACTAMAT.2016.02.050.

[44] L. Lutterotti, S. Gialanella, X-ray diffraction characterization of heavily deformed metallic specimens, Acta Mater. 46 (1998) 101–110. https://doi.org/10.1016/S1359-6454(97)00222-X.

[45] M.J. Starink, Analysis of aluminium based alloys by calorimetry: quantitative analysis of reactions and reaction kinetics, Int. Mater. Rev. 49 (2004) 191–226. https://doi.org/10.1179/095066004225010532.

[46] A. Sergueeva, V. Stolyarov, R. Valiev, A. Mukherjee, Advanced mechanical properties of pure titanium with ultrafine grained structure, Scr. Mater. 45 (2001) 747–752. https://doi.org/http://dx.doi.org/10.1016/S1359-6462(01)01089-2.

[47] R.Z. Valiev, R.K. Islamgaliev, I. V Alexandrov, Bulk nanostructured materials from severe plastic deformation, Prog. Mater. Sci. 45 (2000) 103–189.

https://doi.org/http://dx.doi.org/10.1016/S0079-6425(99)00007-9.

[48] A. Apolinário, C.T. Sousa, J. Ventura, J.D. Costa, D.C. Leitão, J.M. Moreira, J.B. Sousa, L. Andrade, A.M. Mendes, J.P. Araújo, The role of the Ti surface roughness in the self-ordering of TiO_2 nanotubes: a detailed study of the growth mechanism, J. Mater. Chem. A. 2 (2014) 9067–9078. https://doi.org/10.1039/C4TA00871E.

[49] A. Apolinário, P. Quitério, C.T. Sousa, J. Ventura, J.B. Sousa, L. Andrade, A.M. Mendes, J.P. Araújo, Modeling the growth kinetics of anodic TiO_2 nanotubes, J. Phys. Chem. Lett. 6 (2015) 845–851. https://doi.org/10.1021/jz502380b.

[50] J. Liu, P.M. Hosseinpour, S. Luo, D. Heiman, L. Menon, D.A. Arena, L.H. Lewis, TiO_2 nanotube arrays for photocatalysis: Effects of crystallinity, local order, and electronic structure, J. Vac. Sci. Technol. A Vacuum, Surfaces, Film. 33 (2015) 021202. https://doi.org/10.1116/1.4902350.

[51] J. Hedlund, S. Mintova, J. Sterte, Controlling the preferred orientation in silicalite-1 films synthesized by seeding, Microporous Mesoporous Mater. 28 (1999) 185–194. https://doi.org/https://doi.org/10.1016/S1387-1811(98)00300-X.

[52] O.K. Varghese, D. Gong, M. Paulose, C.A. Grimes, E.C. Dickey, Crystallization and high-temperature structural stability of titanium oxide nanotube arrays, J. Mater. Res. 18 (2003) 156–165. https://doi.org/doi:10.1557/JMR.2003.0022.

[53] B. Ohtani, Y. Ogawa, S. Nishimoto, Photocatalytic Activity of Amorphous−Anatase Mixture of Titanium(IV) Oxide Particles Suspended in Aqueous Solutions, J. Phys. Chem. B. 101 (1997) 3746–3752. https://doi.org/10.1021/jp962702+.

[54] H.J. Martin, K.H. Schulz, K.B. Walters, Piranha Treated Titanium Compared to Passivated Titanium as Characterized by XPS, Surf. Sci. Spectra. 15 (2008) 23–30. https://doi.org/10.1116/11.20070702.

[55] S.P. Albu, H. Tsuchiya, S. Fujimoto, P. Schmuki, TiO_2 Nanotubes - Annealing Effects on Detailed Morphology and Structure, Eur. J. Inorg. Chem. 2010 (2010) 4351–4356. https://doi.org/10.1002/ejic.201000608.

[56] D. Yu, X. Zhu, Z. Xu, X. Zhong, Q. Gui, Y. Song, S. Zhang, X. Chen, D. Li, Facile Method to Enhance the Adhesion of TiO_2 Nanotube Arrays to Ti Substrate, ACS Appl. Mater. Interfaces. 6 (2014) 8001–8005. https://doi.org/10.1021/am5015716.

[57] M. Sun, D. Yu, L. Lu, W. Ma, Y. Song, X. Zhu, Effective approach to strengthening TiO_2 nanotube arrays by using double or triple reinforcements, Appl. Surf. Sci. 346 (2015) 172–176. https://doi.org/10.1016/J.APSUSC.2015.04.004.

[58] S.J. Bull, E.G. Berasetegui, An overview of the potential of quantitative coating adhesion measurement by scratch testing, Tribol. Int. 39 (2006) 99–114. https://doi.org/10.1016/J.TRIBOINT.2005.04.013.

[59] X. Liu, P.K. Chu, C. Ding, Surface modification of titanium, titanium alloys, and related materials for biomedical applications, Mater. Sci. Eng. R Reports. 47 (2004) 49–121. https://doi.org/10.1016/j.mser.2004.11.001.

[60] D.M. Brunette, P. Tengvall, M. Textor, P. Thomsen, Titanium in Medicine: Material Science, Surface Science, Engineering, Springer-Verlag, 2001. https://doi.org/10.1007/978-3-642-56486-4.

[61] D. Fang, Z. Luo, K. Huang, D.C. Lagoudas, Effect of heat treatment on morphology, crystalline structure and photocatalysis properties of TiO_2 nanotubes on Ti substrate and freestanding membrane, Appl. Surf. Sci. 257 (2011) 6451–6461. https://doi.org/10.1016/j.apsusc.2011.02.037.

[62] J.M. Macak, A. Ghicov, R. Hahn, H. Tsuchiya, P. Schmuki, Photoelectrochemical properties of N-doped self-organized titania nanotube layers with different thicknesses, J. Mater. Res. 21 (2006) 2824–2828. https://doi.org/10.1557/jmr.2006.0344.

[63] D.A.H. Hanaor, C.C. Sorrell, Review of the anatase to rutile phase transformation, J. Mater. Sci. 46 (2011) 855–874. https://doi.org/10.1007/s10853-010-5113-0.

[64] H. Xie, T. Xi, Q. Zhang, Q. Wu, Study on the Phase Transformation Behavior of Nanosized Amorphous TiO_2, Mater. Sci. Technol. 19 (2003). http://www.jmst.org/CN/abstract/article_6613.shtml.

[65] H. Habazaki, M. Uozumi, H. Konno, K. Shimizu, P. Skeldon, G.E. Thompson, Crystallization of anodic titania on titanium and its alloys, Corros. Sci. 45 (2003) 2063–2073. https://doi.org/10.1016/S0010-938X(03)00040-4.

[66] Y.J. Chen, Y.J. Li, J.C. Walmsley, N. Gao, H.J. Roven, M.J. Starink, T.G. Langdon, Microstructural heterogeneity in hexagonal close-packed pure Ti processed by high-pressure torsion, J. Mater. Sci. 47 (2012) 4838–4844. https://doi.org/10.1007/s10853-012-6343-0.

[67] Y.T. Zhu, J.Y. Huang, J. Gubicza, T. Ungár, Y.M. Wang, E. Ma, R.Z. Valiev, Nanostructures in Ti processed by severe plastic deformation, J. Mater. Res. 18 (2003) 1908–1917. https://doi.org/DOI: 10.1557/JMR.2003.0267.

[68] G.K. Williamson, R.E. Smallman, III. Dislocation densities in some annealed and cold-worked metals from measurements on the X-ray debye-scherrer spectrum, Philos. Mag. A J. Theor. Exp. Appl. Phys. 1 (1956) 34–46. https://doi.org/10.1080/14786435608238074.

[69] S. Leonardi, V. Russo, A. Li Bassi, F. Di Fonzo, T.M. Murray, H. Efstathiadis, A. Agnoli, J. Kunze-Liebhäuser, TiO_2 Nanotubes: Interdependence of Substrate Grain Orientation and Growth Rate, ACS Appl. Mater. Interfaces. 7 (2015) 1662–1668. https://doi.org/10.1021/am507181p.

[70] K. Lu, Z. Tian, J.A. Geldmeier, Polishing effect on anodic titania nanotube formation, Electrochim. Acta. 56 (2011) 6014–6020. https://doi.org/http://dx.doi.org/10.1016/j.electacta.2011.04.098.

[71] N. Hu, N. Gao, M.J. Starink, The influence of surface roughness and high pressure torsion on the growth of anodic titania nanotubes on pure titanium, Appl. Surf. Sci. 387 (2016) 1010–1020. https://doi.org/10.1016/j.apsusc.2016.07.036.

[72] J.M. Macak, M. Jarosova, A. Jäger, H. Sopha, M. Klementová, Influence of the Ti microstructure on anodic self-organized TiO_2 nanotube layers produced in ethylene glycol electrolytes, Appl. Surf. Sci. 371 (2016) 607–612. https://doi.org/10.1016/J.APSUSC.2016.03.012.

[73] U. Diebold, The surface science of titanium dioxide, Surf. Sci. Rep. 48 (2003) 53–229. https://doi.org/http://dx.doi.org/10.1016/S0167-5729(02)00100-0.

[74] X.Q. Gong, A. Selloni, Reactivity of Anatase TiO_2 Nanoparticles: The Role of the Minority (001) Surface, J. Phys. Chem. B. 109 (2005) 19560–19562. https://doi.org/10.1021/jp055311g.

[75] O. Khatim, M. Amamra, K. Chhor, A.M.T. Bell, D. Novikov, D. Vrel, A. Kanaev, Amorphous-anatase phase transition in single immobilized TiO_2 nanoparticles, Chem. Phys. Lett. 558 (2013) 53–56. https://doi.org/10.1016/j.cplett.2012.12.019.

[76] B. Wu, C. Guo, N. Zheng, Z. Xie, G.D. Stucky, Nonaqueous Production of Nanostructured Anatase with High-Energy Facets, J. Am. Chem. Soc. 130 (2008) 17563–17567. https://doi.org/10.1021/ja8069715.

[77] S.M. Baek, M.H. Shin, J. Moon, H.S. Jung, S.A. Lee, W. Hwang, J.T. Yeom, S.K. Hahn, H.S. Kim, Superior pre-osteoblast cell response of etched ultrafine-grained titanium with a controlled crystallographic orientation, Sci. Rep. 7 (2017). https://doi.org/10.1038/srep44213.

[78] R.Z.Z. Valiev, I.P.P. Semenova, V.V.V. Latysh, H. Rack, T.C. Lowe, J. Petruzelka, L. Dluhos, D. Hrusak, J. Sochova, Nanostructured Titanium for Biomedical Applications, Adv. Eng. Mater. 10 (2008) B15–B17. https://doi.org/10.1002/adem.200800026.

[79] S.C. Bellemare, M. Dao, S. Suresh, Effects of mechanical properties and surface friction on elasto-plastic sliding contact, Mech. Mater. 40 (2008) 206–219. https://doi.org/10.1016/j.mechmat.2007.07.006.

[80] S. Bagherifard, R. Ghelichi, A. Khademhosseini, M. Guagliano, Cell Response to Nanocrystallized Metallic Substrates Obtained through Severe Plastic Deformation, ACS Appl. Mater. Interfaces. 6 (2014) 7963–7985. https://doi.org/10.1021/am501119k.

[81] A.J. Engler, S. Sen, H.L. Sweeney, D.E. Discher, Matrix Elasticity Directs Stem Cell Lineage Specification, Cell. 126 (2006) 677–689.

https://doi.org/10.1016/j.cell.2006.06.044.